An asymmetric helicase dimer drives 3′-to-5′ DNA unwinding in type II Druantia antiphage defence

Jun Hou [a,1], Xin Yi [a,1], Wen-Wen Kong [b,1], Yuxin Yang [a], Fengzhi Yuan [a], Peijia Li [a], Hanzhong Feng [a], Zhuangzhuang Chu [a], Long Gui [b *], Yong-Xing He [a,c *]

[a] Ministry of Education Key Laboratory of Cell Activities and Stress Adaptations, School of Life Sciences, Lanzhou University, Lanzhou, 730000, China.

[b] Shenzhen Medical Academy of Research and Translation, Shenzhen, Guangdong, China.

[c] State Key Laboratory for Animal Disease Control and Prevention, College of Veterinary Medicine, Lanzhou University, Lanzhou Veterinary Research Institute, Chinese Academy of Agricultural Sciences, Lanzhou 730000, China.

[1] These authors contributed equally to this work.

[*] Correspondence: guilong@smart.org.cn; heyx@lzu.edu.cn.

Keywords: Druantia | Antiviral defence | Helicase | Cryo-EM | Mechanochemical coupling | Steric exclusion

Abstract

Druantia systems are widespread antiphage defence systems organized around the conserved helicase DruE. However, how DruE recognizes DNA substrates and executes phage restriction has remained unclear, particularly for type II Druantia systems that encode DruE together with DruM, DruF, and DruG. Here we show that DruE from the type II Druantia system of *Pseudomonas protegens* is a DNA-stimulated ATPase and 3′-to-5′ helicase that preferentially engages substrates with an exposed 3′ single-stranded entry strand at a duplex junction, such as 3′-overhang and forked DNA. Seven cryo-EM structures, including an apo dimer and six DNA-bound nucleotide states, define a nucleotide-resolved structural trajectory for substrate loading, motor remodeling, displaced-strand capture, and DNA unwinding. DruE forms an asymmetric homodimer in which one protomer functions as the tracking-strand motor, whereas the second engages the displaced strand and adjacent

duplex in a clamp-like configuration. A fork-junction anchor, a nucleotide-gated lid, an Arg1422-associated contact switch, and inter-protomer contacts together explain how ATP turnover is coupled to directional unwinding. Because DruE recognizes fork-like DNA structures that may also arise during host DNA replication or repair, its activity likely requires regulation. Consistent with this idea, mitomycin C (MMC) sensitivity phenotypes suggest that the type II accessory proteins DruM, DruF, and DruG may regulate DruE activity or limit self-toxicity. Together, these results define a mechanochemical model for type II DruE and support a model in which Druantia targets 3′-ended or fork-like phage replication intermediates to suppress infection.

Significance Statement

Many bacterial and eukaryotic immune systems are built around helicases, yet it remains difficult to see how these enzymes turn ATP hydrolysis into the directional, processive DNA unwinding that drives antiviral defence. We determined seven cryo-EM structures of DruE, the effector of a type II Druantia system, that together span the reaction from substrate binding through the hydrolysis step, giving a nearly complete view of one unwinding cycle. DruE forms a stable asymmetric homodimer, present in our preparations even in the absence of substrate. One subunit moves along the DNA and separates the strands, while the second holds the displaced strand and keeps the enzyme engaged. The structures explain how the motor steps in one direction and how it may distinguish phage DNA from the host chromosome.

Introduction

Bacteriophages are ubiquitous and continually impose selective pressure on bacteria and archaea, fueling a sustained co-evolutionary arms race (1). To counter phage predation, prokaryotes deploy a diverse repertoire of antiviral defences. Alongside classic restriction–modification (2) and CRISPR–Cas systems (3), comparative genomic mining has recently revealed a rapidly expanding arsenal of innate mechanisms (4). These include cyclic-oligonucleotide–based signaling pathways (CBASS) (5), retron-based abortive infection modules (6, 7), Gabija (8), and RADAR (9, 10), among many others. These systems participate in a wide array of antiphage processes—spanning nucleic-acid surveillance, second-messenger signaling, and programmed cell death (abortive infection) (11)—underscoring the extraordinary breadth and dynamics of host–phage interactions.

As the exploration of prokaryotic immunity unfolds, helicase-containing defence systems have emerged as a particularly prominent and mechanistically intriguing class. Superfamily 1 (SF1) and superfamily 2 (SF2) represent the largest groups of helicases, characterized by a conserved ATP-dependent core of RecA-like domains that unwind nucleic acids with strict polarity, while accessory domains diversify substrate recognition and regulation (12). Recent surveys indicate that ~20% of non–restriction-modification defence loci encode an SF1/SF2 helicase (13), highlighting their frequent repurposing as molecular hubs for sensing and executing antiviral responses. For instance, in the Hachiman system, the Ski2-like DNA helicase HamB continuously surveys intracellular DNA; recognition of exposed 3′ overhangs, which can arise from host-genome damage or phage DNA replication, triggers mechanochemical ratcheting that allosterically activates the HamA nuclease, culminating in indiscriminate DNA degradation and abortive infection (14). In DISARM, the DrmAB complex is autoinhibited by a trigger loop that is dislodged upon binding to the DNA substrates with a 5′ overhang, initiating long-range activating rearrangements (15, 16). Despite these advances, a fundamental paradox remains: how do these powerful mechanochemical motors strictly differentiate between viral replication intermediates and the host genome, and crucially, how do they avoid illicit unwinding of intact self-DNA to prevent catastrophic autoimmunity?

Among these defence systems, Druantia is a widespread multi-gene operon recently identified through large-scale genomic mining (9). Druantia systems encode a large, conserved SF2 helicase, DruE (1800–2100 aa), alongside highly variable, subtype-specific accessory genes. Four major subtypes (I–IV) have been described: type I systems encode four accessory genes (DruA–D), type II (*Pseudomonas protegens* Pf-5) encode three (DruM/F/G), type III encode a single accessory gene (DruH), and type IV encode three (DruF/L/K) (17) (Fig. 1A). DruE belongs to the widespread YprA helicase family, characterized by an N-terminal helicase core followed by an oligonucleotide/oligosaccharide-binding (OB) domain, a connector (CON) domain, and a zinc-coordinating DUF1998 domain. Recent comprehensive phylogenomic analyses have identified YprA-family helicases as the central evolutionary "missing link" connecting diverse defence systems, including DISARM and Druantia (18). However, despite this recognized centrality, how Druantia-specific helicases and their accessory partners structurally sense infection and execute defence remained poorly understood, particularly for the multigene type II system.

Here, we elucidate the functional and structural basis of broad-spectrum antiphage immunity mediated by the Druantia effector DruE. Using in vivo

genetic dissection combined with an MMC-induced DNA damage model (19), we establish DruE as an effector whose toxicity is associated with compromised genome integrity and is restrained by the DruM/F/G accessory components. Biochemically, DruE operates as a strictly polarized 3′→5′ mechanochemical motor with a distinct preference for 3′-overhangs. By capturing a continuum of seven high-resolution cryo-EM conformational states (states I–VII), we reveal that upon substrate engagement, DruE engages substrate as a stable asymmetric homodimer and drives unwinding through an ATP-dependent cycle in which the two protomers take distinct roles. Whereas recently described type III Druantia systems appear to disassemble or otherwise remodel their DruE dimer upon activation, here the central two-fold symmetry of the DruE homodimer imposes topological constraints within its central channel that we interpret as a "steric exclusion" barrier to the 5′ strand. We propose that this barrier helps dictate substrate polarity and may limit unwinding of the intact host genome. Together, our findings suggest how the type II Druantia system integrates damage-associated substrate recognition, ATP-driven mechanochemical activity, and accessory-protein regulation to restrict phage infection while limiting self-toxicity.

Results

Functional Characterization of the Type II Druantia System

To evaluate the antiphage activity of the Type II Druantia system, we heterologously expressed the *Pseudomonas protegens* Pf-5 *druMFGE* operon in *Escherichia coli*. While DruM and DruE were expressed as soluble proteins, DruF and DruG accumulated in the insoluble fraction, hindering the reconstitution of an active type II Druantia system in *E. coli* (Fig. S1). Because DruM is a DNA methyltransferase typically implicated in self/non-self discrimination rather than direct viral clearance (20), we investigated whether the helicase effector DruE alone suffices to mediate phage defence. When challenged with a panel of five bacteriophages (T1, T4, T5, T7, and λ), heterologous expression of DruE conferred robust protection specifically against T1 and T7 (Fig. 1B, Fig. S2). This defence phenotype was significantly abolished by an alanine substitution of a critical arginine residue (R1241A) within the highly conserved motif VI of the RecA2 domain, a putative "arginine finger" essential for coupling ATP hydrolysis to mechanical transduction (21). These data demonstrate the essential role of DruE in antiphage function (Fig. 1C).

To dissect the functional contribution of individual genes within the *druMFGE* locus, we generated single, in-frame deletion mutants (*ΔdruM*, *ΔdruF*, *ΔdruG* and *ΔdruE*). Under standard growth conditions, all mutant strains exhibited growth kinetics comparable to the wild-type strain (Fig. S5). Intriguingly, upon exposure to MMC, a DNA-damaging agent that induces replication fork stalling (22), deletion of *druE* markedly alleviated MMC-induced toxicity. In contrast, deletion of *druM*, *druF*, or *druG* hypersensitized the host strains to MMC (Fig. 1D). Collectively, these findings suggest that DruE acts as a genotoxically activated toxic effector, whereas DruM, DruF, and DruG may cooperatively safeguard the host against DruE-mediated autoimmunity (23).

Biochemical Characterization of DruE as a 3′-to-5′ Helicase

To elucidate the molecular mechanism underlying DruE-mediated antiviral toxicity in vito, we biochemically characterized the enzymatic profile and substrate specificity of purified recombinant DruE. In vitro reconstitution assays revealed that DruE possesses robust, DNA-dependent ATPase activity (Fig. 2A). Notably, this ATP hydrolytic activity was preferentially stimulated by double-stranded DNA (dsDNA) or structured fork intermediates, whereas single-stranded DNA (ssDNA) or the absence of DNA elicited negligible stimulation, indicating that the ATPase motor is strictly gated by duplex DNA or junction-specific features to prevent futile energy consumption on single-stranded templates. Next, we subjected the enzyme to gel-based helicase assays using diverse DNA substrates featuring distinct junction topologies (Fig. 2B–E). DruE efficiently unwound DNA substrates harboring a 3′ single-stranded DNA overhang or a Y-fork junction in an ATP-dependent manner (Fig. 2B, D). In contrast, the enzyme was inactive against substrates with 5′ overhangs or blunt-ended duplexes (Fig. 2C, E). This strict requirement for a 3′ ssDNA entry portal, a classic molecular hallmark of stalled replication forks or genotoxic intermediates (24, 25), classifies DruE as a dedicated 3′-to-5′ helicase. These biochemical attributes align well with the previous inference that DruE was a genotoxically activated toxic effector (Fig. 1B).

Overall structure of DruE

To elucidate the molecular basis of DruE-mediated DNA unwinding, we determined the cryo-EM structures of DruE bound to a forked (Y-shaped) DNA substrate — a 70-bp duplex flanked by a 21-nt 3′ and a 6-nt 5′ single-stranded arm — in the presence of

Mg^{2+} and either ADP or the non-hydrolyzable analog AMP-PNP. Single-particle analysis of the ADP sample resolved a DNA-free apo dimer (3.64 Å) and two substrate-bound DruE–DNA–ADP dimers (3.29 and 3.45 Å), whereas the AMP-PNP sample yielded four substrate-bound dimers trapped in distinct conformations (3.28–3.58 Å) (Fig. 3B, Figs. S3 and S4; Tables S1 and S2). Local-resolution analyses and representative model-to-map fits for the AMP-PNP and ADP reconstructions are provided in Fig. S8 and Fig. S9, respectively. Only part of the forked substrate was ordered, and the extent of ordered DNA varied across the structures: the duplex flanking the fork junction and the 3′ tracking strand were modelled in most maps, the 5′ displaced strand was resolved in only a subset, and in one reconstruction the duplex was not resolved at all, leaving only the single-stranded tracking strand threaded through one protomer. As these maps capture the enzyme before, during, and after the catalytic step, they provide the basis for the architectural description below and for the mechanistic analysis in the following sections.

DruE can be divided into multiple structural domains. Its catalytic core comprises two RecA-like domains, RecA1 and RecA2. In contrast to canonical SF2 helicases (12), in which each RecA domain forms a contiguous module, both RecA1 and RecA2 domains of DruE are interrupted by large insertions: RecA1 is split by an anchoring loop (Anc-L) contacting the DNA duplex and an α-helical insertion (α-Ins), while the RecA2 segment sequentially incorporates a first zinc-binding module (ZBM1), a MarR-like domain, and a second zinc-binding module (ZBM2) (Fig. 3A). Despite this discontinuous primary sequence of the RecA domains, the interleaved segments fold into a single, intact helicase core. At the C-terminal to the helicase core, DruE comprises a third zinc-binding module (ZBM3), an α-helical domain, an OB-fold tethered to the core through an extended 'Rope' linker, a connector (CON) domain, a DUF1998 domain which is also a zinc-binding module named ZBM4, and a terminal iVsr domain (18, 26). Spatially, the α-Ins and the α-helical domain are tightly packed around the RecA1 domain (Fig. 3C). In contrast, the MarR-like domain, the zinc-binding insertions, the OB-fold, the CON domain, the DUF1998 module, and the iVsr module are primarily arranged around the RecA2 domain, collectively expanding the helicase core (Fig. 3D).

DruE is a homodimer in every reconstruction, including the apo form, indicating that dimerization is constitutive rather than substrate-induced. The two protomers are related by an approximate two-fold axis, with their MarR-like domains contributing to the dimer interface. In the DNA-bound reconstructions, they engage a forked DNA substrate asymmetrically. The duplex arm of the fork contacts the dimer, and at the fork the two strands separate. Each single strand is then threaded into a different protomer through a distinct entry point, with protomer A binding the 5′ displaced strand and

protomer B the 3′ tracking strand (Fig. 3C, D). The two protomers are therefore conformationally non-equivalent in every state, forming an asymmetric dimer in which each captures a strand of defined polarity. As shown below, this arrangement underlies DruE's alternating unwinding cycle and its strict strand selectivity.

A junction anchor is essential for coupling ATP hydrolysis to DNA unwinding

As an SF2 helicase, DruE powers DNA unwinding by converting cycles of ATP binding and hydrolysis into directional movement along the tracking strand. This coupling requires two elements acting in concert: a catalytic site that hydrolyzes the nucleotide, and protein–DNA contacts that transmit the accompanying conformational changes as mechanical force. To define the structural basis of this coupling in DruE, we examined its nucleotide-binding site and its contacts with the DNA in turn.

The nucleotide-binding site lies in the cleft between RecA1 and RecA2 (Fig. 4A). The nucleotide and the catalytic Mg^{2+} are coordinated by conserved motifs from both lobes. In RecA1, the Walker A motif (Motif I; Lys140) coordinates the phosphates, while the Q motif reads out the adenine base, conferring specificity for ATP (21). Within this motif, Tyr110 and Tyr113 sandwich the adenine, each stacking against one face (Fig. 4C), and Gln116 hydrogen-bonds to it. Meanwhile, the arginine finger of Motif VI (Arg1241) reaches across the cleft from RecA2 (Fig. 4B). Consistent with their catalytic role, alanine substitution of the nucleobase-sensing Gln116, the phosphate-coordinating Lys140, or the trans-acting Arg1241 each abolished both ATP hydrolysis and DNA unwinding, whereas the stacking tyrosines were largely dispensable, with Y110A retaining essentially wild-type activity and Y113A causing only a modest reduction (Fig. 4G).

Whereas the ATPase site governs the chemistry, a separate element couples it to unwinding at the fork. In protomer A, an insertion within RecA1 engages the forked DNA (Fig. 4E): a flexible loop (residues 161–192) contacts the duplex arm through Lys176 and Arg178 (Fig. 4D), while an adjacent α-helix reaches the fork junction through Lys261 and contacts the displaced strand through Arg269 (Fig. 4F). Of these contacts, only the junction substitution K261A abolished unwinding, whereas the duplex substitutions (K176A, R178A) and the displaced-strand substitution (R269A) had little effect (Fig. 4H). In contrast to the ATPase-site mutants, K261A retained wild-type ATPase activity despite its complete loss of unwinding (Fig. 4I). This uncoupling identifies Lys261,

positioned at the fork junction, as the anchor that converts ATP hydrolysis into productive unwinding: when it is removed, the motor continues to hydrolyse ATP but no longer separates the two strands (12).

Two dimer interfaces with distinct roles in the DruE helicase

As a constitutive dimer, DruE must both restrain and coordinate its two protomers. The dimer interface is formed by the MarR-like domains of the two protomers, which clasp one another through two distinct contacts: a peripheral Interface I and a more deeply buried, central Interface II (Fig. 5B). Interface I is a hydrogen-bond network between antiparallel α-helices, one from each MarR-like domain, including Glu880 and Lys885 (Fig. 5F). Interface II forms the central, buried contact between the two MarR-like domains, including His966 and Lys1033 (Fig. 5F). These contacts account for the MarR-like contribution to dimerization noted earlier (20).

Substitutions in the two interfaces had contrasting effects. Disrupting Interface I (E880A, K885A) left DNA unwinding intact but raised ATPase activity above the wild-type level (Fig. 5D, E), suggesting that Interface I may help restrain the motor in the resting state and limit unproductive hydrolysis. In contrast, the Interface II substitution K1033A abolished unwinding while leaving ATPase activity unaffected (Fig. 5D, E), indicating that Interface II is not part of the catalytic site but is instead required to couple ATP hydrolysis to unwinding. Together, these data point to distinct contributions from the two interfaces: Interface I may impose an autoinhibitory restraint, whereas Interface II is needed to the helicase activity of DruE (12).

An asymmetric, nucleotide-gated cycle drives stepwise translocation

To follow how the DruE dimer translocates along DNA, we determined seven conformational states of DruE: an apo (DNA-free, nucleotide-free) reference (state I) and six DNA-bound states (states II–VII; Fig. 6A). In every DNA-bound state protomer B threads the 3′ tracking strand through its central channel. The six states sample different combinations of nucleotide occupancy in the two protomers, each captured in a distinct conformation. These structural snapshots allowed us to separate the contributions of the two protomers and to build a model for how DruE steps along DNA (14).

We first compared state II, in which only protomer B engages the ssDNA, with the apo reference (state I). ssDNA binding drives a large conformational change in protomer B, whereas protomer A is essentially unchanged (Fig. 6B, C). In protomer B the rearrangement is concentrated in ZBM1 (residues 596–801), which undergoes a substantial displacement as it reorganizes to engage the tracking strand (Fig. 6E, H). Over the same transition the C-terminal module of protomer B, spanning the OB, ZBM3, and CON domains and the DUF1998/ZBM4 module (residues 1416–1721), becomes disordered and is not resolved in the state II map, indicating that this region is mobile when ssDNA is bound but nucleotide is absent (Fig. 6B, C). Local analysis of ZBM1 showed that it gates the DNA at the entry to the channel. In the states in which the C-terminal module is disordered (states II and V), a defined stretch of the tracking strand nonetheless remains held within the central channel (Fig. S6A, B, D, E). This stretch is anchored by Arg785, which lies in a ZBM1 loop rich in basic residues that lines a positively charged path for the DNA. Arg785 contacts the substrate through electrostatic interactions and hydrogen bonds and holds the tracking strand in place, so that it does not slide back or release while the C-terminal module is mobile. In contrast, the displaced strand, which lacks comparable contacts in this region of the channel, shows no ordered density and is disordered. Consistent with this role, an alanine substitution of Arg785 (R785A) abolished unwinding (Fig. S6B, C, E, F; Fig. 6K).

We next compared state III, in which protomer B is bound to AMP-PNP while protomer A remains empty, with state II. AMP-PNP binding to protomer B triggers a clear rearrangement of the core motor: the RecA1 domain and the domains packed against it shift toward the DNA-exit side of the channel, drawing the bound tracking strand forward into the interior of the dimer. This nucleotide-dependent shift of the RecA1 nucleotide pocket provides the power stroke that advances the substrate along the unwinding path (Fig. 6F, I). At the same time, the whole of protomer B becomes well-resolved, including the previously disordered 1416–1721 module, and the bound 3′-overhang substrate is now clearly ordered in the map. AMP-PNP binding therefore drives the 1416–1721 module from a flexible to a stably ordered state. Because this module closes over the tracking strand, we refer to it as the lid (Fig. 6D, F) (16). When comparing state IV with state III, we found that, although protomer B is nearly identical in the two states (overall RMSD 0.508 Å), one loop at the N-terminal edge of the lid (residues 1419–1422) rearranges between the AMP-PNP (state III) and ADP (state IV) states. In the pre-hydrolysis state III, Arg1422 hydrogen-bonds to Glu1501 in ZBM3. After hydrolysis, in state IV, the loop swings so that Arg1422 instead contacts Gln1666 in DUF1998/ZBM4 (Fig. 6G, J,

M). Because this toggle is coupled to the chemical step, we propose that it acts as a ratchet that biases translocation in a single direction. Consistent with a central role for this loop, substitution of Arg1422 or the nearby Pro1420 abolished unwinding, which was accompanied by a reduction in the ATPase activity of the Arg1422 mutant (Fig. 6K, L), whereas substitution of the immediately adjacent Met1419 had little effect (Fig. 6K).

We next examined states V, VI, and VII, in which protomer A is nucleotide-bound (AMP-PNP in states V and VI, ADP in state VII) and has captured the 5′ displaced strand. In these structures a greater length of the substrate's duplex arm (the not-yet-unwound region) is resolved, and the strand of this duplex continuous with the displaced strand contacts the anchoring loop of protomer A, an interaction absent from states II–IV, where less of the duplex was ordered (Fig. S7A–F). Comparing protomer A across states V–VII with states I–IV, a large conformational change extends over residues 1286–1921, spanning the α-helical domain, the OB, ZBM3, and CON domains, DUF1998/ZBM4, and iVsr, which together make up essentially the entire C-terminal region of the protomer. Capture of the displaced strand widens the DNA-binding channel of protomer A, and nucleotide binding reshapes and widens its nucleotide-binding pocket (Fig. S7G–L). Together these coupled changes suggest that nucleotide stabilizes the displaced-strand-bound conformation of protomer A and strengthens the grip of DruE on its substrate, which would in turn enhance processivity. Consistent with a contribution of this grip to unwinding, alanine substitution of the anchoring-loop residues Lys176 and Arg178 reduced unwinding (Fig. 4H). Over the same three states protomer B reproduces almost exactly the conformational series of states II–IV, with its lid open when nucleotide-free (state V) and closed when AMP-PNP (state VI) or ADP (state VII) is bound, independently of the nucleotide state of protomer A (Fig. 7A).

Together these structures suggest a model in which the two protomers of DruE play asymmetric roles in unwinding. Protomer B is the translocating engine. Loading begins when a free 3′ single-stranded end threads into it and opens the lid, so only a substrate with an accessible 3′ overhang can be loaded. Nucleotide binding then closes the lid over the tracking strand, enclosing it in a sealed channel, and hydrolysis drives the Arg1422 toggle, which we propose acts as a ratchet that biases translocation in one direction. Because our reconstructions are static, the stepping itself is inferred rather than observed: we propose that protomer B advances along the tracking strand in steps coupled to lid closure, with their direction set by this hydrolysis-coupled ratchet. Protomer A, by contrast, appears not to be a second engine but a

processivity clamp: it captures the 5′ displaced strand and grips the adjacent duplex arm through its anchoring loop, with nucleotide stabilizing this grip. Because the protomers are gated independently, protomer B can cycle regardless of the nucleotide state of protomer A, so the two need not move in synchrony. In this model the directional stepping of protomer B separates the strands at the fork while protomer A retains the displaced strand, allowing DruE to unwind the forked substrate processively from its 3′ overhang (Fig. 7A) (15).

Discussion

Druantia systems are widespread antiphage defence systems organized around the conserved SF2/MrfA-YprA-family helicase DruE. Here, seven cryo-EM structures of type II DruE, including one DNA-free state and six DNA-bound nucleotide states, define a structural trajectory for substrate loading, nucleotide-dependent remodeling, and 3′-to-5′ DNA unwinding. These structures are not isolated snapshots, but instead capture two related conformational series that together describe much of a proposed unwinding cycle. This nucleotide-resolved view extends general principles of SF2 helicase translocation into the context of antiphage immunity and provides a mechanistic framework for understanding how immune helicases act on phage-derived DNA intermediates [5,10,13,18,22].

A central feature of the seven structures is the asymmetric DruE dimer. Protomer B threads the 3′ tracking strand through the helicase channel and undergoes the major nucleotide-dependent rearrangements, identifying it as the translocating motor. Protomer A contacts the 5′ displaced strand and adjacent duplex, forming a clamp-like element that may stabilize the fork and limit reannealing. States II-IV describe motor cycling before stable displaced-strand capture, whereas states V-VII capture related nucleotide states after protomer A has gripped the displaced strand. Thus, displaced-strand capture appears to add a substrate-retention module without replacing the nucleotide cycle of the motor protomer. The nucleotide-gated lid, the Arg1422-associated contact switch, Lys261 at the fork junction, and asymmetric inter-protomer contacts together explain how ATP turnover is coupled to directional unwinding (Fig. 7A).

The biochemical data further distinguish DNA-stimulated ATPase activation

from productive strand separation. Several duplex-containing substrates activate ATP turnover, but efficient unwinding requires an exposed 3′ single-stranded entry strand at a duplex junction. Such 3′-ended or fork-like structures can arise during phage genome replication, including cohesive-end processing, rolling-circle replication, recombination intermediates, and branched or stalled replication forks, which are vulnerable DNA structures frequently associated with replication stress and recombination-dependent repair (24). MMC induces DNA interstrand crosslinks and DNA-damage responses that interfere with DNA strand separation and replication, thereby creating replication-stress conditions relevant to fork-like DNA intermediates (27–29). The opposing phenotypes produced by druE and the accessory genes druM, druF, and druG under MMC treatment therefore suggest that the type II Druantia locus is tuned to DNA-stress physiology. We propose that DruF and DruG may regulate DruE activity, substrate licensing, or system homeostasis, whereas DruM may represent a putative SAM-dependent methylation-related module. However, because DruM, DruF, and DruG have not yet been reconstituted with DruE, their precise roles remain unresolved (Fig. 7B).

Together, our structures and biochemical analyses support a model in which type II DruE recognizes 3′-ended or fork-like phage replication intermediates and suppresses genome amplification through ATP-dependent unwinding. This model is consistent with the broader idea that bacterial defence systems can target vulnerable stages of phage DNA replication, while also emphasizing the need for regulation to avoid deleterious activity on host DNA. The seven-state DruE trajectory therefore provides a framework for understanding how immune helicases convert nucleotide-state changes into antiphage DNA remodeling. More broadly, these findings raise two central questions for Druantia and related defence systems: how DruE is licensed during infection, and how its unwinding activity is converted into irreversible phage restriction.

Materials and Methods

Experimental models and bacterial strains

For standard cultivation, all *Escherichia coli* strains were grown in Luria-Bertani (LB) medium at 37 °C with shaking at 220 r.p.m. Antibiotics were supplemented as required for plasmid maintenance (e.g., ampicillin at 100 μg/mL). Bacterial strains were stored at -80 °C as 25% (v/v) glycerol stocks. *E. coli* DH5α was used for plasmid cloning and amplification, whereas *E. coli* BL21 (DE3) and *E. coli* BL21 were employed for protein expression and phage

infection assays, respectively. Phages T1 (11303-B1), T4, T5, T7, and λ were generously provided by the Ning Jia lab at the Southern University of Science and Technology. Phage propagation followed standard protocols, typically infecting logarithmically growing host cells in LB medium at 37 °C with an initial multiplicity of infection (MOI) of 0.1. Phage titers were determined using the double-layer agar plate method. All strains, plasmids, and phages used in this study are detailed in the Supplementary Table S6.

Construction of mutation strains

The in-frame deletion mutants were generated using a two-step homologous recombination approach as previously described. Briefly, ~1 kb flanking regions upstream and downstream of the target gene were amplified by PCR using high-fidelity DNA polymerase. These two fragments were fused by overlap extension PCR and then cloned into the suicide vector pK18mobsacB. The resulting recombinant plasmid was transformed into *E. coli* WM3064 and subsequently transferred into the recipient strain via conjugation on LB agar supplemented with 0.3 mM DAP. The single-crossover transconjugants were first selected on LB agar containing kanamycin and then cultured in LB broth without antibiotics to allow for the second crossover. Subsequently, the cultures were spread onto LB agar supplemented with 10% sucrose to counter-select against vector retention via the sacB gene; sucrose-resistant colonies were screened and successful deletion mutants were validated by PCR using target gene primers.

Identification and visualization of Druantia loci

Based on DefenseFinder (4) annotations, Druantia loci and their neighboring defence systems were identified in the genomes of Serratia fonticola (GCF_005489985.1), Pseudomonas protegens Pf-5 (GCF_000012265.1), Klebsiella michiganensis (GCF_002025225.1), and Metabacillus litoralis SW-211 (GCF_007994985.1). Genomic operons were visualized using the Python library dna_features_viewer (28), coupled with pandas for data processing and matplotlib for auxiliary plotting.

Plasmid construction and protein purification

All novel plasmids generated in this study were constructed utilizing PCR, gel extraction (Omega Bio-tek, D2500-02), and either Gibson assembly (30) or Golden Gate assembly (31). DNA templates for the amplification of wild-type and mutant Druantia loci were derived from the *P. protegens* Pf-5 genome (extracted using the TIANGEN Bacterial Genomic DNA Extraction Kit). Fragments encompassing the wild-type and mutant DruE genes and their corresponding point mutants (K176A, R178A, K261A, R269A, E880A, K885A, H966A, K1033A…) were cloned into respective vectors.

For protein expression, *E. coli* BL21 (DE3) cells harboring the pETDuet-1-*druE* plasmid were inoculated into 1 L of LB medium and cultured at 37 °C until the OD600 reached 0.6–0.8. Protein expression was induced with 0.5 mM IPTG at 16 °C overnight (16 hours). Cells were harvested, resuspended in lysis buffer (20 mM Tris-HCl pH 8.0, 500 mM NaCl), and lysed via sonication (70% amplitude, 1 s on, 2 s off, 20 min total). Following high-speed centrifugation (12,000 × g, 45 min), the supernatant was collected and applied to Strep-Tactin 4FF affinity resin (Smart Lifesciences, Changzhou, China). After washing out non-specifically bound proteins, the target protein was eluted using a buffer supplemented with 2.5 mM desthiobiotin. The eluate was then concentrated and injected onto a pre-equilibrated Superdex 200 10/300 GL size-exclusion chromatography column (Cytiva) for polishing, using chromatography buffer (20 mM Tris-HCl pH 8.0, 150 mM NaCl). The oligomeric state was evaluated based on the elution volume (indicating a homodimer of approximately 400 kDa). The peak fractions were pooled, flash-frozen in liquid nitrogen, and stored at -80 °C. Mutant proteins were purified following the identical protocol as the wild type.

Efficiency of plating determination

To determine the efficiency of plating (EOP), phages were plated on the induced strains containing the DruE and compared to the plating on control strain BL21. For this, 200 µL of bacterial culture was mixed with a countable number of infectious particles (50–150 PFU/plate) and 4.5 mL of 0.6% LBA prewarmed at 45 °C. The mixture was then poured on top of a LBA plate to form a bacterial layer containing the infectious particles. After overnight incubation at 37 °C, the EOP was calculated by dividing the number of plaques counted on each plate by the number of plaques formed in the control strain.

DNA substrate preparation

All single-stranded oligonucleotides, including those with 5′-FAM fluorescent modifications, were synthesized by GENEWIZ (Tianjin, China). To prepare various double-stranded DNA (dsDNA) substrates (e.g., blunt-ended, 3′-overhang, 5′-overhang, and Y-fork), single-stranded oligonucleotides were mixed with equimolar or a 1.5-fold excess of their complementary strands in annealing buffer (20 mM Tris-HCl pH 7.5, 50 mM NaCl, 5 mM MgCl2). Annealing was facilitated by heating the mixture to 95 °C for 5 minutes, followed by a gradual cooling to 25 °C over 110 minutes. The purity of the annealed products was verified by 8% native polyacrylamide gel electrophoresis (PAGE) (32). Sequences of all substrates are detailed in Supplementary Table S5.

Cryo-EM sample preparation and data collection

To capture the DruE complex during DNA unwinding, a Y-fork DNA construct was designed, comprising a 19-bp stem region, a 6-nt 5′-overhang, and a 20-nt 3′-overhang (33, 34)(Table S5, Fig. S3A). This specific substrate was selected as it has been widely utilized to trap unwinding intermediates of bacterial SF2 helicase complexes. Purified DruE (5 μM) was incubated with a 10-fold molar excess of DNA substrate (50 μM) and a 100-fold excess of ADP (0.5 mM; Macklin Biochemical, Shanghai, China). Following a 30-minute incubation at room temperature (~25 °C), 4 μL of the DruE–DNA–ADP mixture was applied to glow-discharged holey carbon grids (Copper, 300 mesh, R1.2/1.3, Quantifoil). The grids were blotted for 4 s at 4 °C under 100% humidity using a Vitrobot Mark IV (FEI Company) and rapidly plunge-frozen in liquid ethane.

Cryo-EM data were acquired on a Krios G4 transmission electron microscope operating at 300 kV, equipped with a Falcon4i direct electron detector and a Selectris X energy filter (slit width: 10 eV). Movie stacks were collected in electron event representation (EER) mode using EPU software (Thermo Fisher Scientific), with a total electron dose of 50 $e^{-}/Å^{2}$ and a defocus range of -0.8 μm to -1.6 μm. Sample preparation and data collection for the DruE–DNA–AMP-PNP complex were performed identically to those for the ADP state.

Cryo-EM image processing

All cryo-EM data processing was performed in cryoSPARC (35).Preprocessing and particle picking: All datasets were collected with a pixel size of 0.96 Å/pixel. Beam-induced motion correction of movie stacks was performed using the Patch Motion Correction module, and contrast transfer function (CTF) parameters were estimated via Patch CTF Estimation. Initial particle picking was conducted using Blob Picker with an un-binned box size of 400 pixels, followed by 2D classification of 2× and 4× down-sampled particles to generate reference templates. Subsequently, template-based picking was executed on the motion-corrected and CTF-estimated micrographs utilizing Template Picker.

Processing of the DruE–DNA–ADP complex: For this dataset (Fig. S3), a total of 4,571 movie stacks were collected. Template Picker yielded an initial set of 2,542,668 particles. These particles were subjected to *ab initio* reconstruction (C1 symmetry), generating 5 classes. To eliminate "junk" classes, three rounds of heterogeneous refinement (box size 128 pixels, forced hard classification) were performed. This process isolated 417,803 high-quality 'passthrough' particles, yielding a consensus reconstruction with a gold-standard Fourier shell correlation (GSFSC) overall resolution of 3.31 Å. The consensus particle set was further subjected to non-uniform refinement, incorporating per-

particle defocus optimization, global CTF refinement (tilt, trefoil, and spherical aberration), noise model initialization from images, and local motion correction. A subsequent round of heterogeneous refinement (box size 128 pixels, initial resolution 6 Å) successfully classified the particles into three distinct conformational states: State I (27,065 particles, 3.64 Å), State IV (73,269 particles, 3.45 Å), and State VII (210,656 particles, 3.29 Å).

Processing of the DruE–DNA–AMP-PNP complex: For this dataset (Fig. S4), 6,752 movie stacks were collected. Following a parallel processing pipeline, 1,928,979 particles were initially picked. After *ab initio* reconstruction (5 classes) and three rounds of heterogeneous refinement to filter out "junk" particles, 616,796 high-quality particles were retained, yielding a consensus reconstruction at 3.26 Å resolution. Following an identical non-uniform refinement strategy, heterogeneous refinement classified the dataset into four distinct states: State II (233,472 particles, 3.28 Å), State III (136,706 particles, 3.36 Å), State V (138,033 particles, 3.45 Å), and State VI (50,310 particles, 3.58 Å).

Local refinement and post-processing: To enhance the local density quality surrounding the ATP-binding site, local refinement was performed using a mask focused on this region. The resulting refined 3D volumes were subsequently post-processed using EMReady2 (36) to facilitate model building.

Model building and refinement

The initial model of DruE was generated using AlphaFold2 (37). For model building, the predicted model was rigid-body fitted into the experimental cryo-EM density maps using the fitmap tool in UCSF ChimeraX v1.10.1 (38). Given the significant conformational disparities between the prediction and the experimental structure, multiple rounds of manual, iterative building were performed utilizing Coot (39), the ISOLDE plugin (40), and Phenix (41). This initially refined DruE structure subsequently served as the baseline model for all other conformational states. The DNA substrate, zinc ion (Zn^{2+}), and nucleotide ligands (ADP or AMP-PNP) were built *de novo* in Coot based on the experimental density. Finally, all atomic models underwent real-space refinement using phenix.real_space_refine, and the overall geometric quality was evaluated using MolProbity (42).

NTPase activity assays

The ATPase activity of DruE was evaluated by quantifying the release of inorganic phosphate using a Malachite Green Phosphate Assay Kit (Beyotime) according to the manufacturer's instructions (43). Reactions were carried out

in a buffer containing 20 mM Tris-HCl pH 7.5, 50 mM KCl, 2 mM MgCl2, and 1 mM DTT. Assays were performed in transparent-bottom, black 96-well plates. DruE was diluted to a final concentration of 40 nM, and the nucleic acid substrate (Table S5) was diluted to 100 nM (or plasmid DNA to a final concentration of 4 ng/μL), in a total reaction volume of 10 μL. The reaction mixture was pre-incubated at room temperature for 5 minutes. ATP (Macklin Biochemical, Shanghai, China) was then added to a final concentration of 1 mM to initiate the reaction, followed by incubation at 37 °C for 30 minutes. The reaction was quenched by the addition of the activated Malachite Green reagent. After a 30-minute colorimetric development in the dark at room temperature, the absorbance at 620 nm was measured using a BioTek microplate reader. Phosphate release was quantified by interpolation from a standard curve of free phosphate. The oligonucleotide substrates utilized in this assay were adapted from classical previous studies.

Gel-shift helicase unwinding assays

Helicase unwinding reactions were performed in Isothermal Amplification Buffer (IAB) at 30 °C. DruE (100 nM) was pre-incubated with 20 nM of fluorescently labeled DNA substrate (Table S3) for 5 minutes. The reaction was initiated by the addition of 1 mM ATP or AMP-PNP (Macklin Biochemical). At 20 min, aliquots were transferred to ice and quenched with a STOP buffer (containing 0.4 U Proteinase K, 18 mM EDTA, 0.36% SDS, and 9% glycerol). To prevent re-annealing of the unwound DNA strands, a 2-fold molar excess of unlabeled trap oligonucleotide (identical in sequence to the fluorescently labeled single strand) was added during the quenching step. For the fully unwound control (Boiled control), the substrate was boiled at 95 °C for 5 minutes and loaded immediately. All samples were resolved on a 12% TBE polyacrylamide gel at 4 °C until the bands were adequately separated. The gel was then scanned using a multifunctional laser imaging and automated gel excision system (Bio-Rad/BIO-LAB PharosFX), and images were exported with Image Lab software.

Construction of single-gene knockout mutants and phenotypic assays

To elucidate the *in vivo* function of the Druantia system within its native host, *P. protegens* Pf-5, we employed a homologous recombination strategy to independently delete the four core genes (*druM*, *druF*, *druG*, and *druE*). This resulted in the successful generation of four single-gene knockout mutant strains (designated Δ*druM*, Δ*druF*, Δ*druG*, and Δ*druE*).

Following overnight culture, the wild-type (WT) Pf-5 strain and the knockout

mutants were subcultured at a 1:100 ratio into fresh liquid medium. Upon reaching an OD600 of 0.2, the treatment groups were supplemented with Mitomycin C (MMC; Aladdin Biochemical Technology, Shanghai, China) to a final concentration of 2 μg/mL, alongside an equivalent volume of vehicle for the control groups. The cultures were transferred to 96-well plates, and growth kinetics were continuously monitored by measuring the OD600 utilizing a BioTek microplate reader. All assays were performed in triplicate as independent biological replicates. Statistical analysis was conducted using GraphPad Prism 9.

Data Availability

All data supporting the findings of this study are available within the paper and its Supplementary Information. For the DruE–DNA–ADP complex, the cryo-EM density maps for the three conformational states (State I, State IV, and State VII) have been deposited in the Electron Microscopy Data Bank (EMDB) under accession codes EMD-65815 (State I), EMD-65907 (State IV), and EMD-65816 (State VII); the corresponding atomic models have been deposited in the Protein Data Bank (PDB) under accession codes 9WAE (State I), 9WDV (State IV), and 9WAF (State VII). The consensus reconstruction density map is available under EMD-65895, and the locally refined maps for the State I state under EMD-65813 and EMD-65814.

For the DruE–DNA–AMP-PNP complex, the density maps for the four states (State II, State III, State V, and State VI) are deposited under EMDB accession codes EMD-65906 (State II), EMD-65908 (State III), EMD-65901 (State V), and EMD-65910 (State VI); the corresponding PDB models under 9WDU (State II), 9WDW (State III), 9WDS (State V), and 9WDY (State VI). The consensus and locally refined maps for the State II state are deposited under EMD-65902, EMD-65903, and EMD-65904; and those for the State V state under EMD-65897, EMD-65898, and EMD-65899.

Acknowledgements

We gratefully acknowledge Dr. Gang Fu for technical support during cryo-EM image acquisition. We also thank the Structural Biology Core Facility at the Bio-Tech Center of SMART for technical assistance. Additionally, we acknowledge the Computing Labware for Electron Microscopy Visualization and Experimental Research (CLEVER) at SMART for support with data analysis.

Figure Legends

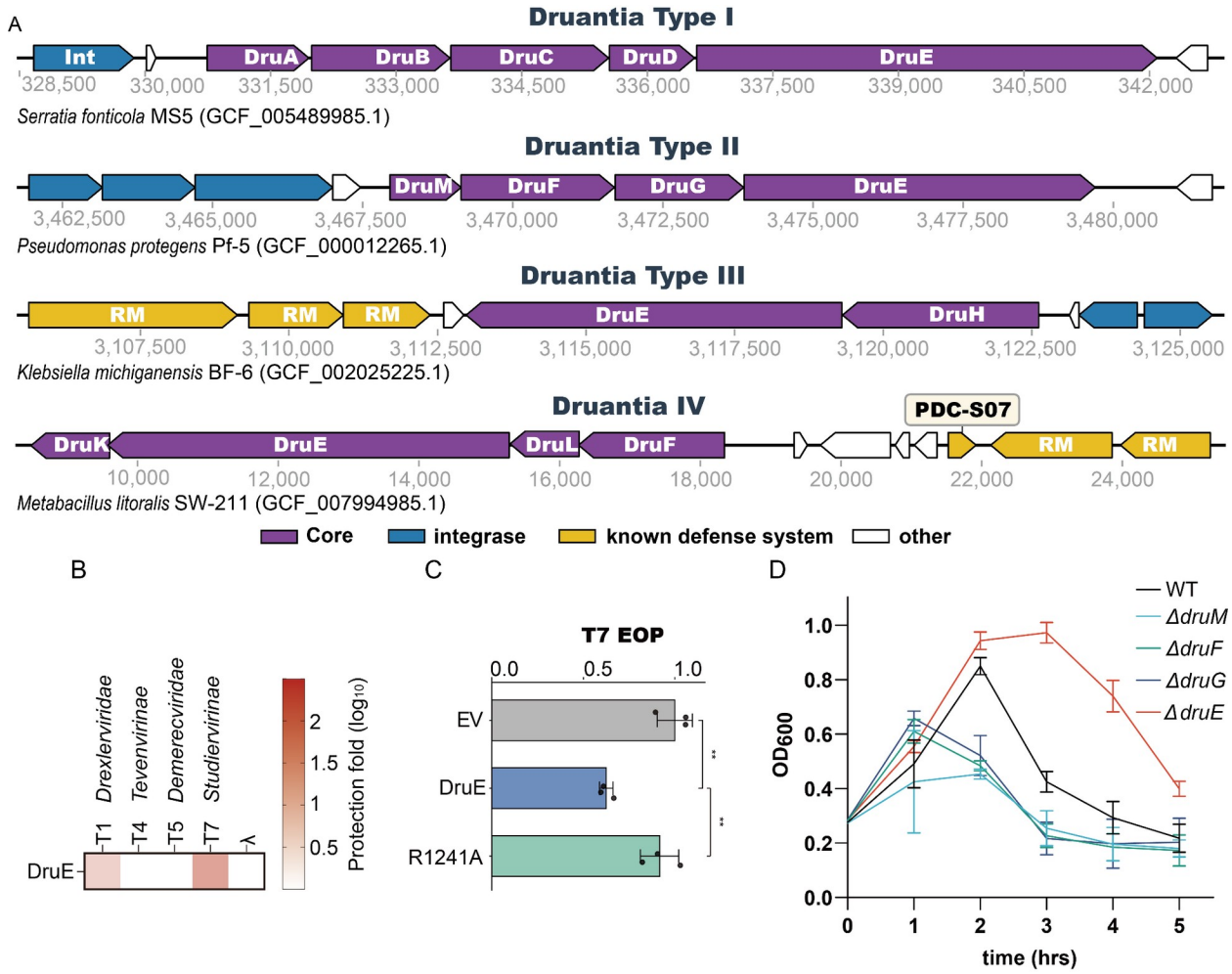

Figure 1. Genomic organization and functional characterization of the Druantia defence systems. (A) Schematic representation of the genomic loci for the four major subtypes (Types I–IV) of the Druantia defence system. Genes are colored by functional categories: purple for core genes (including the conserved SF2 helicase DruE), blue for integrases, yellow for other known defence systems, and white for other adjacent genes. Bacterial strains and NCBI assembly accessions are indicated below each locus. (B) Phage protection profile of the Pseudomonas protegens Pf-5 DruE effector expressed in Escherichia coli against a panel of five bacteriophages (T1, T4, T5, T7, and λ). The heatmap indicates the protection fold (log10 (C) Efficiency of plating (EOP) of phage T7 on E. coli strains expressing empty vector (EV), wild-type DruE, or the catalytic mutant DruE (R1241A). **(C)** Efficiency of plating (EOP) of phage T7 on *E. coli* expressing empty vector (EV), wild-type DruE, or the catalytic-site mutant DruE R1241A. Bars represent the mean ± SD from three independent biological replicates. Pairwise comparisons are indicated by brackets; $P < 0.05$, **P** < 0.01, and ***P*** < 0.001. (D) Growth curves of P. protegens Pf-5 wild-type (WT) and single-gene deletion strains (ΔdruM, ΔdruF, ΔdruG, and Δ druE) following exposure to mitomycin C (MMC). Optical density at 600 nm (OD600) was monitored over a 5-hour time course. Data represent mean ± SD.

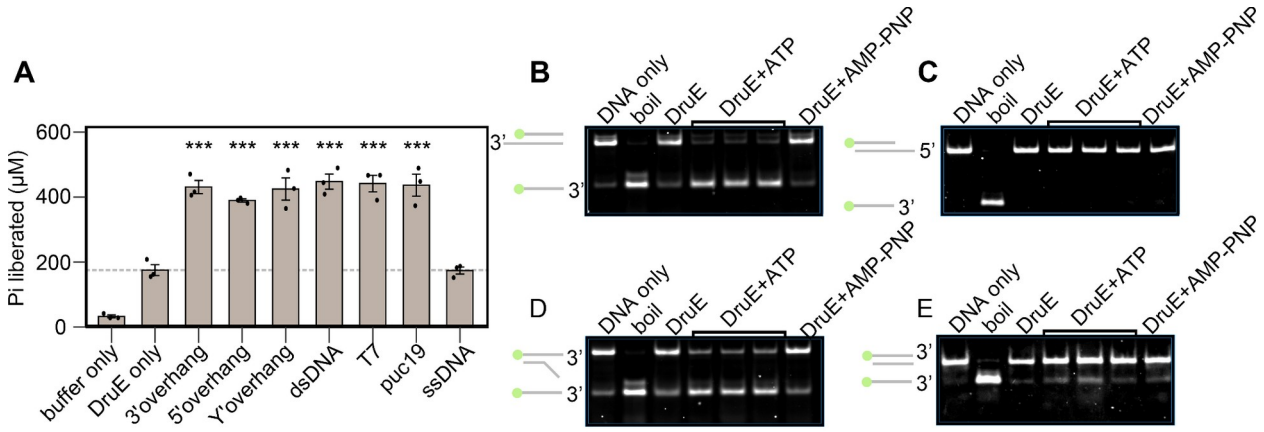

Figure 2. Biochemical characterization of the DNA-dependent ATPase and 3′-to-5′ helicase activities of DruE. (A) ATPase activity of purified recombinant DruE in the absence or presence of the indicated DNA substrates: 3′-overhang, 5′-overhang, Y-fork, double-stranded DNA (dsDNA), T7 genomic DNA, pUC19 plasmid DNA, and single-stranded DNA (ssDNA). ATPase activity was quantified by measuring the concentration of released inorganic phosphate (Pi). Bars represent the mean ± SD from three independent experiments. Statistical significance relative to the DruE-only control is indicated by asterisks (**P < 0.01; ***P < 0.001). (B-E) Gel-based helicase assays using a 3′-overhang substrate (B), a 5′-overhang substrate (C), a Y-fork substrate (D), or a blunt-ended duplex substrate (E). Substrate diagrams are shown to the left of each panel. Reactions contained DNA substrate alone, boiled substrate as a denaturation control, DruE without nucleotide, DruE with the indicated concentrations of ATP, or DruE with the nonhydrolyzable ATP analog AMP-PNP. All reactions were incubated for 20 min.

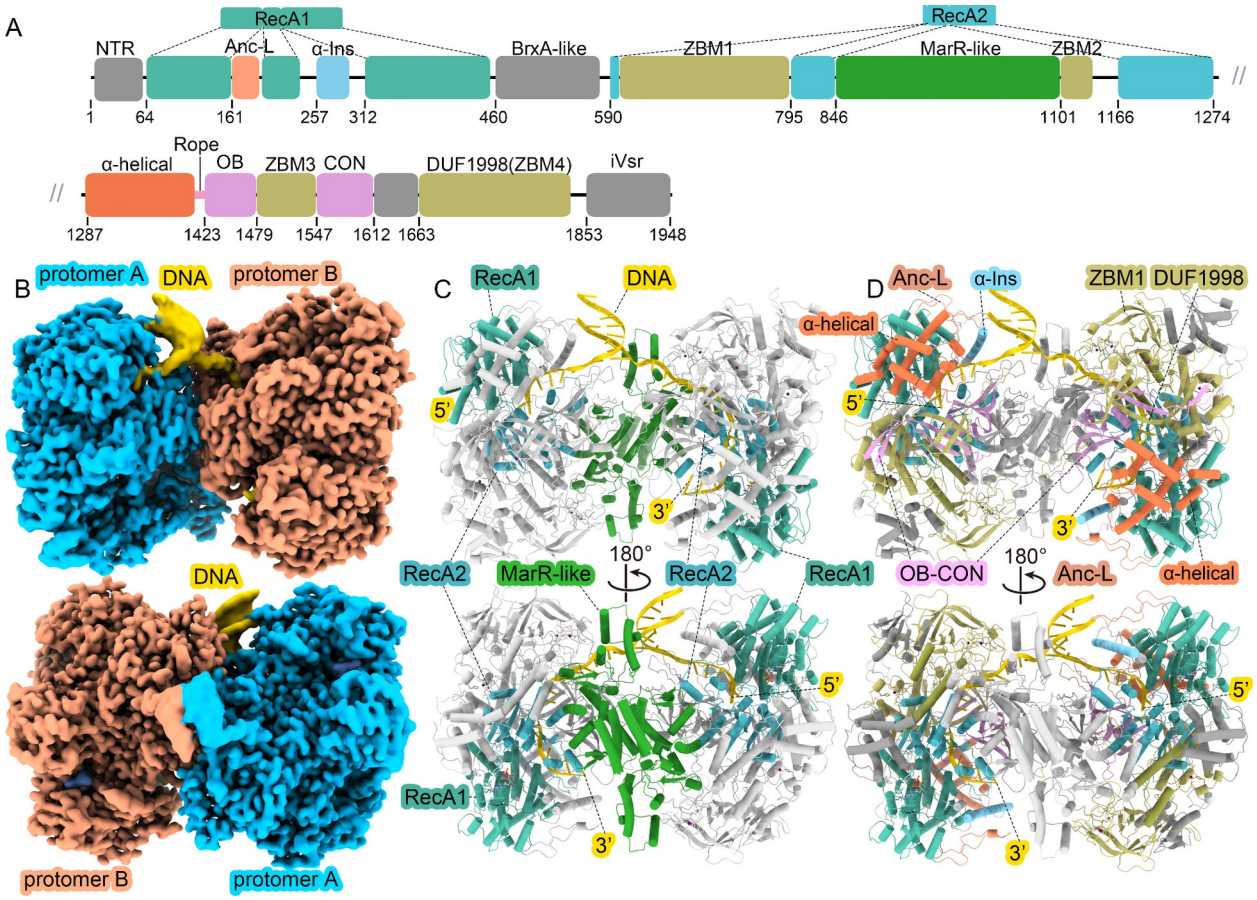

Figure 3. Domain architecture and dimeric structure of DruE bound to a forked DNA. (A) Linear domain organization of DruE. The polypeptide chain is color-coded by structural domains with amino acid boundaries indicated below. The catalytic core consists of two discontinuous RecA-like domains (RecA1 and RecA2) interrupted by large insertions: an anchoring loop (Anc-L) and an α-helical insertion (α-Ins) within RecA1; and a zinc-binding module 1 (ZBM1), a MarR-like domain, and ZBM2 within RecA2. The C-terminal region contains an α-helical domain, an OB-fold connected via a 'Rope' linker, a connector (CON) domain, a DUF1998 module (ZBM4), and an iVsr domain. (B) Cryo-EM density maps (top: front view; bottom: 180° rotated view) of the asymmetric DruE homodimer bound to a forked DNA (yellow). Protomer A and protomer B are colored blue and wheat, respectively. (C, D) Ribbon diagrams showing the asymmetric interaction with the forked DNA substrate, rotated by 180° (top vs. bottom). Panel C highlights the assembly of the discontinuous RecA1 (teal) and RecA2 (green) domains into an intact helicase core, with the MarR-like domains mediating the dimer interface. Panel D highlights the spatial distribution of the insertions and C-terminal domains around the helicase core. The duplex DNA is unwound at the junction, with the 5′ displaced strand threaded into protomer A and the 3′ tracking strand into protomer B.

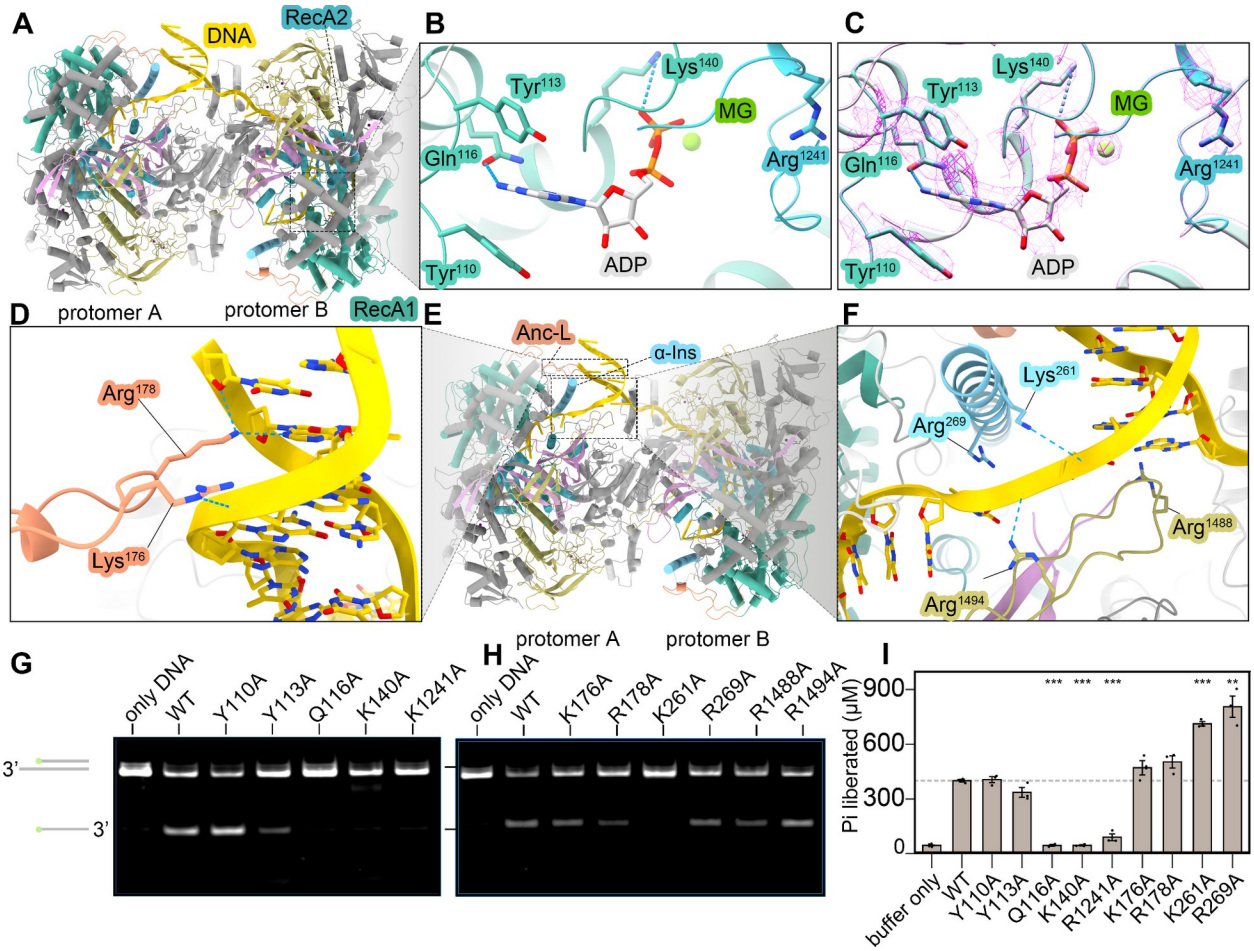

Figure 4. Structural basis of nucleotide recognition and mechanochemical coupling by DruE. (A) Overall view of the nucleotide-binding pocket located in the cleft between the RecA1 and RecA2 domains. (B) Close-up view of the catalytic site showing the coordination of ADP and Mg^{2+}. Tyr110, Tyr113, Gln116, Lys140, and the putative arginine finger Arg1241 are shown as sticks, with hydrogen bonds indicated by blue dashed lines. (C) Representative cryo-EM density map, shown as a magenta mesh, surrounding the atomic model of ADP, Mg^{2+}, and the interacting residues displayed in B. (D) Close-up view of the anchoring loop (Anc-L), showing interactions of Lys176 and Arg178 with the duplex DNA. (E) Overview of the DruE-DNA interaction interface, highlighting the Anc-L and α-helical insertion (α-Ins) in protomer A. (F) Close-up view of the α-Ins at the fork junction. Lys261 contacts the fork junction, whereas Arg269 engages the displaced strand; additional DNA contacts involving Arg1488 and Arg1494 are also indicated. (G) Gel-based helicase assays comparing wild-type (WT) DruE with alanine-substitution mutants of residues involved in nucleotide binding and ATPase activity. (H) Gel-based helicase assays comparing WT DruE with alanine-substitution mutants of residues at the DNA-binding interface. DNA alone serves as the negative control in G and H. (I) DNA-stimulated ATPase activities of WT DruE and the indicated mutants, quantified by measuring the concentration of released inorganic phosphate (Pi). Bars represent the mean ± SD from three independent experiments. Statistical significance relative to WT is indicated by asterisks (**P < 0.01; ***P < 0.001). Notably, K261A retained DNA-stimulated ATPase activity but lacked detectable unwinding activity, indicating uncoupling of ATP turnover from productive strand separation.

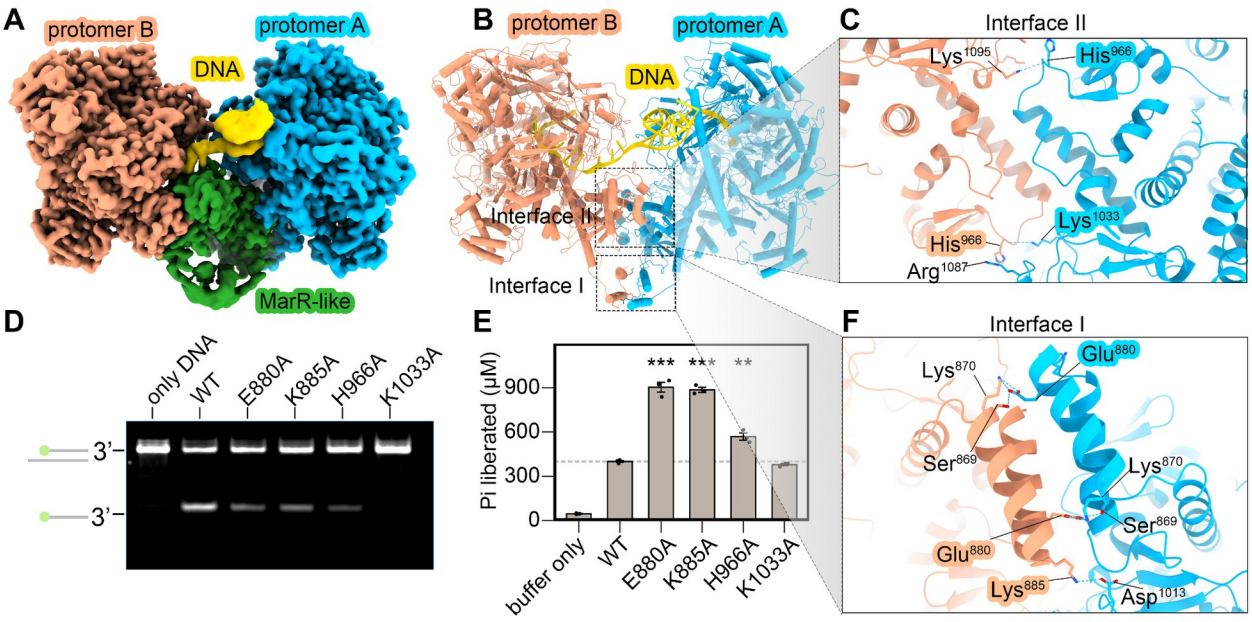

Figure 5. Structural and functional characterization of the DruE dimer interfaces. (A) Cryo-EM density map of the DNA-bound DruE dimer, with protomer A colored cyan, protomer B salmon, the forked DNA yellow, and the MarR-like domains green. (B) Cartoon representation of the DruE-DNA complex showing the locations of two distinct inter-protomer contact regions, the peripheral interface I and central interface II. (C) Close-up view of interface II. Key residues from the two protomers, including His966, Lys1033, Arg1087, and Lys1095, are shown as sticks, with hydrogen bonds and electrostatic interactions indicated by dashed lines. (D) Native PAGE-based helicase assays comparing the 3′-to-5′ DNA-unwinding activities of wild-type (WT) DruE and the indicated alanine-substitution mutants at the dimer interfaces. DNA alone serves as the negative control. (E) DNA-stimulated ATPase activities of WT DruE and the indicated interface mutants, quantified by measuring the concentration of released inorganic phosphate (Pi). Bars represent the mean ± SD from three independent experiments. Statistical significance relative to WT is indicated by asterisks (**P < 0.01; ***P < 0.001). (F) Close-up view of interface I, showing a symmetric interaction network between antiparallel α-helices from the two protomers. Key interacting residues, including Ser869, Lys870, Glu880, Lys885, and Asp1013, are shown as sticks, with hydrogen bonds and electrostatic interactions indicated by dashed lines.

A

Protomer B \ Protomer A	Apo (Nucleotide-free)	DNA + AMP-PNP-bound	DNA + ADP-bound
Apo (Nucleotide-free)	State I	—	—
DNA-bound	State II	State V	—
DNA + AMP-PNP-bound	State III	State VI	—
DNA + ADP-bound	State IV	—	State VII

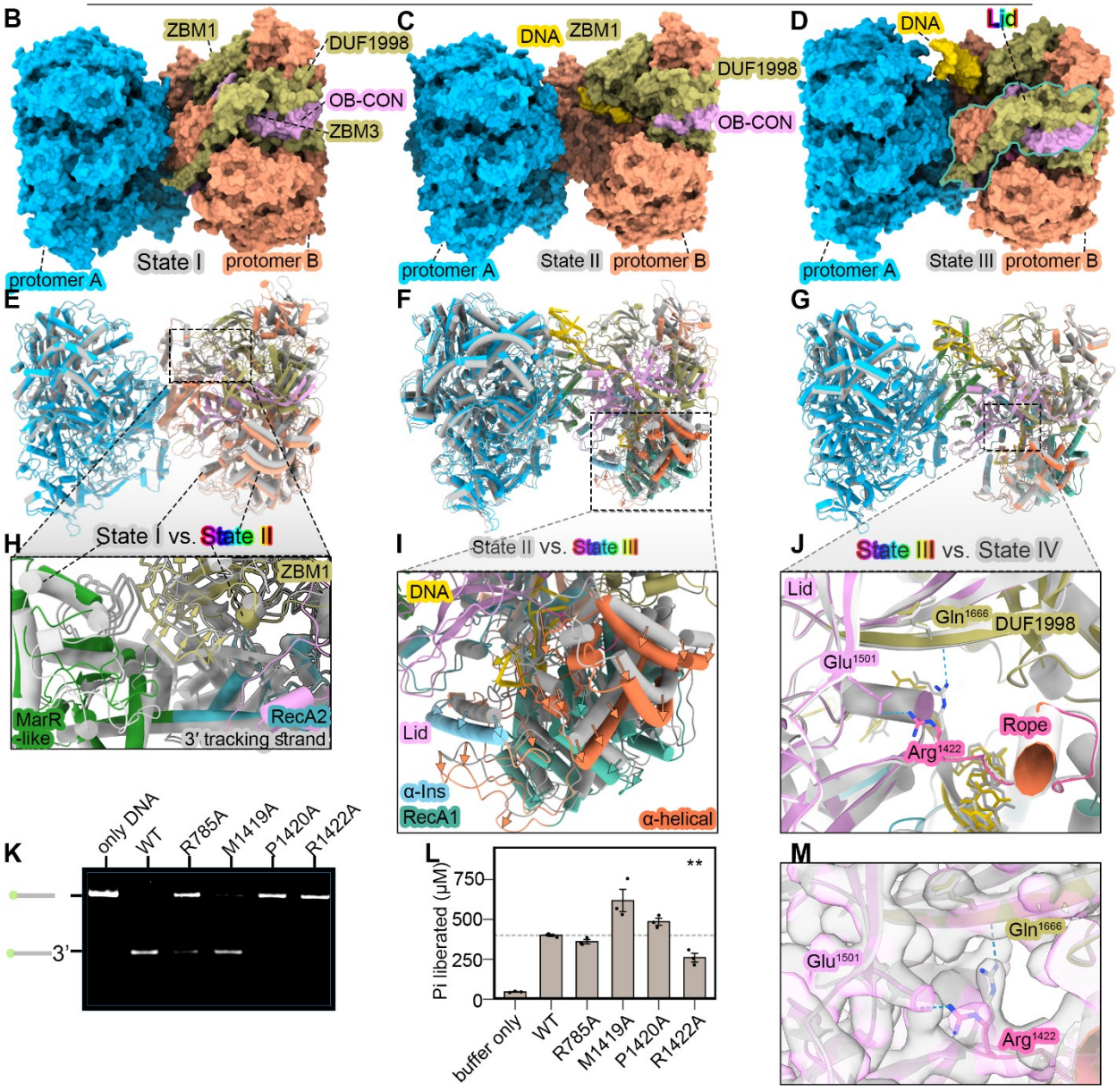

Figure 6. Cryo-EM structures, conformational transitions, and functional verification of DruE during DNA translocation. (A) Schematic table of the seven distinct conformational states captured for DruE, defining the specific combinations of nucleotide occupancy and DNA binding within protomers A and B across States I–VII. (B–D) Surface representations of the atomic models of DruE tracking from State I to State III. (B) State I (apo reference state). (C) State II, showing that the binding of ssDNA exclusively drives a large conformational rearrangement in protomer B, while protomer A remains essentially unchanged. (D) State III, showing that the C-terminal module ("lid") becomes stably ordered and seals the channel upon nucleotide binding. (E) Detailed view at the channel entry of protomer B comparing State II with State I, highlighting the DNA-gating mechanism where the ZBM1 domain (residues 596–801) undergoes a substantial displacement to engage the tracking strand (grey: State I; coloured: State II). (F) Structural alignment between State II (grey) and State III (coloured). AMP-PNP binding to protomer B triggers a prominent power stroke, shifting the core motor domain and drawing the tracking strand forward into the interior of the dimer. (G) Structural superposition of the pre-hydrolysis state (State III, AMP-PNP, colored) and post-hydrolysis state (State IV, ADP, grey), showing that they are nearly identical with an overall RMSD of 0.508 Å. (H) Close-up zoom of panel (E), illustrating the detailed vector displacement trajectories of the ZBM1 domain during substrate gating (grey: State I; coloured: State II). (I) Close-up zoom of panel (F), illustrating the directional trajectories of the RecA1-driven power stroke upon nucleotide binding (grey: State II; coloured: State III). (J) Local close-up zoom of panel (G), revealing the fine structural remodeling (directional toggle) of the ratchet loop containing Arg1422 (grey: State IV; coloured: State III). (K and L) Biochemical validation of key gating and translocation residues. In vitro DNA unwinding assays (K) and relative ATPase activity assays (L) for wild-type (WT) DruE and mutants (R785A, M1419A, P1420A, and R1422A). Alanine substitutions of channel-anchoring residue Arg785, ratchet residue Arg1422, or Pro1420 abolish unwinding activity. Bars represent the mean ± SD from three independent experiments. Statistical significance relative to WT is indicated by asterisks (**$P < 0.01$; ***$P < 0.001$). (M) Close-up cryo-EM density maps corresponding to the local structural toggle in panel (J), explicitly demonstrating the clear density transition and amino acid side-chain rearrangement of Arg1422 and its surrounding contacts between State IV (grey) and State III (coloured).

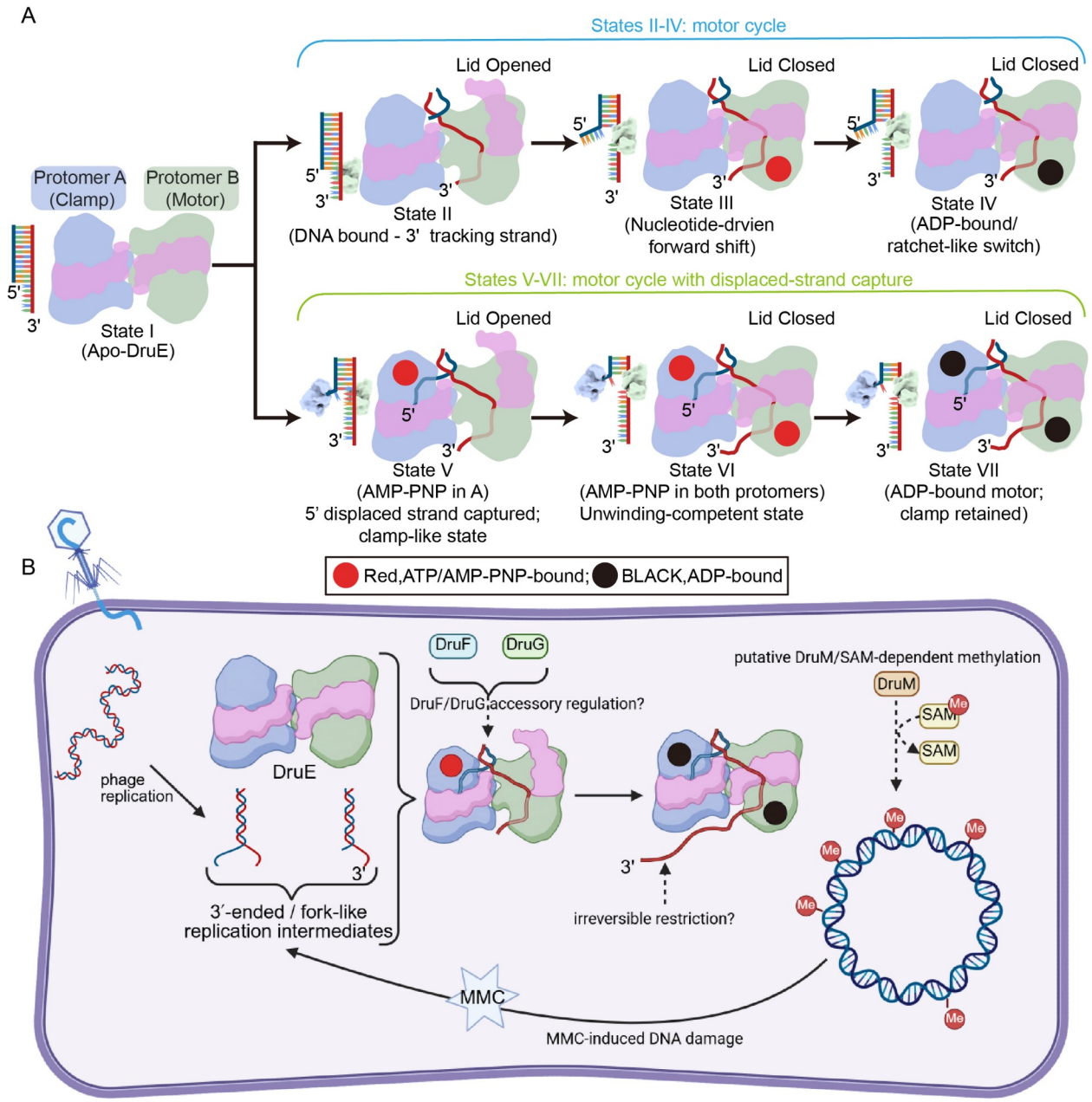

Figure 7. Mechanism of DruE-mediated DNA unwinding and a working model for type II Druantia defence. (A) Proposed mechanochemical cycle of the asymmetric DruE homodimer. DruE recognizes DNA substrates containing an exposed 3′ single-stranded end at a duplex junction, including 3′-overhang and forked DNA. In the apo state, DruE adopts an open conformation (state I). DNA loading threads the 3′ tracking strand into protomer B, the motor subunit, while the nucleotide-gated lid remains open (state II). AMP-PNP binding closes the lid and induces a forward power stroke along the tracking strand (state III). Conversion to the ADP-bound state is accompanied by a hydrolysis-coupled conformational switch that is proposed to bias directional translocation (state IV). During strand separation, protomer A captures the 5′ displaced strand and functions as a processivity clamp. Nucleotide binding stabilizes this displaced-strand-bound state (state V), whereas simultaneous AMP-PNP occupancy of both protomers produces a dual-nucleotide, unwinding-competent state (state VI). Following hydrolysis, both protomers adopt ADP-bound conformations, while protomer A retains the displaced strand to maintain substrate engagement and limit strand re-annealing (state VII). Red and black circles indicate AMP-PNP- and ADP-bound states, respectively. (B) Working model for type II Druantia-mediated antiphage defence. DruE may recognize exposed 3′ single-stranded DNA ends and fork-like intermediates generated during phage genome replication and unwind these substrates in an ATP-dependent 3′–5′ direction, thereby interfering with phage DNA replication. This substrate-recognition and unwinding pathway is supported by biochemical and structural data and is indicated by solid arrows. Genetic analyses under mitomycin C-induced DNA damage suggest that DruE can impose toxicity on the host, whereas DruM, DruF and DruG may limit DruE-associated self-damage or otherwise maintain system homeostasis. Direct regulation of DruE by DruM, DruF or DruG, as well as a protective role for DruM-dependent DNA methylation, has not been experimentally established and is therefore depicted with dashed arrows.

References

1. H. G. Hampton, B. N. J. Watson, P. C. Fineran, The arms race between bacteria and their phage foes. *Nature* **577**, 327–336 (2020).

2. R. J. Roberts, *et al.*, A nomenclature for restriction enzymes, DNA methyltransferases, homing endonucleases and their genes. *Nucleic Acids Res* **31**, 1805–1812 (2003).

3. K. S. Makarova, *et al.*, Evolutionary classification of CRISPR-Cas systems: a burst of class 2 and derived variants. *Nat Rev Microbiol* **18**, 67–83 (2020).

4. F. Tesson, *et al.*, Systematic and quantitative view of the antiviral arsenal of prokaryotes. *Nat Commun* **13**, 2561 (2022).

5. D. Cohen, *et al.*, Cyclic GMP-AMP signalling protects bacteria against viral infection. *Nature* **574**, 691–695 (2019).

6. A. Millman, *et al.*, Bacterial Retrons Function In Anti-Phage

Defense. *Cell* **183**, 1551–1561.e12 (2020).

7. X.-Y. Song, *et al.*, Bacterial reverse transcriptase synthesizes long poly(A)-rich cDNA for antiphage defense. *Science* **388**, eads4639 (2025).

8. S. P. Antine, *et al.*, Structural basis of Gabija anti-phage defence and viral immune evasion. *Nature* **625**, 360–365 (2024).

9. S. Doron, *et al.*, Systematic discovery of antiphage defense systems in the microbial pangenome. *Science* **359** (2018).

10. B. Duncan-Lowey, *et al.*, Cryo-EM structure of the RADAR supramolecular anti-phage defense complex. *Cell* **186**, 987–998.e15 (2023).

11. A. Lopatina, N. Tal, R. Sorek, Abortive Infection: Bacterial Suicide as an Antiviral Immune Strategy. *Annu Rev Virol* **7**, 371–384 (2020).

12. M. E. Fairman-Williams, U.-P. Guenther, E. Jankowsky, SF1 and SF2 helicases: family matters. *Curr Opin Struct Biol* **20**, 313–324 (2010).

13. N. A. O'Leary, *et al.*, Reference sequence (RefSeq) database at NCBI: current status, taxonomic expansion, and functional annotation. *Nucleic Acids Res* **44**, D733–45 (2016).

14. O. T. Tuck, *et al.*, Genome integrity sensing by the broad-spectrum Hachiman antiphage defense complex. *Cell* **187**, 6914–6928.e20 (2024).

15. G. Ofir, *et al.*, DISARM is a widespread bacterial defence system with broad anti-phage activities. *Nat Microbiol* **3**, 90–98 (2018).

16. J. P. K. Bravo, C. Aparicio-Maldonado, F. L. Nobrega, S. J. J. Brouns, D. W. Taylor, Structural basis for broad anti-phage immunity by DISARM. *Nat Commun* **13**, 2987 (2022).

17. L. J. Payne, *et al.*, Identification and classification of antiviral defence systems in bacteria and archaea with PADLOC reveals new system types. *Nucleic Acids Res* **49**, 10868–10878 (2021).

18. R. T. Bell, *et al.*, YprA family helicases provide the missing link between diverse prokaryotic immune systems. *bioRxiv* (2025).

19. M. Filipiak, J. M. Łoś, M. Łoś, Efficiency of induction of Shiga-toxin lambdoid prophages in Escherichia coli due to oxidative and antibiotic stress depends on the combination of prophage and the bacterial strain. *J Appl Genet* **61**, 131–140 (2020).

20. K. Vasu, V. Nagaraja, Diverse functions of restriction-modification

systems in addition to cellular defense. *Microbiol Mol Biol Rev* **77**, 53–72 (2013).

21. M. R. Singleton, M. S. Dillingham, D. B. Wigley, Structure and mechanism of helicases and nucleic acid translocases. *Annu Rev Biochem* **76**, 23–50 (2007).

22. M. Tomasz, Mitomycin C: small, fast and deadly (but very selective). *Chem Biol* **2**, 575–579 (1995).

23. N. Tal, R. Sorek, SnapShot: Bacterial immunity. *Cell* **185**, 578–578.e1 (2022).

24. M. M. Cox, *et al.*, The importance of repairing stalled replication forks. *Nature* **404**, 37–41 (2000).

25. B. Michel, G. Grompone, M.-J. Florès, V. Bidnenko, Multiple pathways process stalled replication forks. *Proceedings of the National Academy of Sciences* **101**, 12783–12788 (2004).

26. J. J. Roske, S. Liu, B. Loll, U. Neu, M. C. Wahl, A skipping rope translocation mechanism in a widespread family of DNA repair helicases. *Nucleic Acids Res* **49**, 504–518 (2021).

27. M. D. Sutton, B. T. Smith, V. G. Godoy, G. C. Walker, The SOS response: recent insights into umuDC-dependent mutagenesis and DNA damage tolerance. *Annu Rev Genet* **34**, 479–497 (2000).

28. A. J. Deans, S. C. West, DNA interstrand crosslink repair and cancer. *Nat Rev Cancer* **11**, 467–480 (2011).

29. B. Michel, After 30 years of study, the bacterial SOS response still surprises us. *PLoS Biol* **3**, e255 (2005).

30. D. G. Gibson, *et al.*, Enzymatic assembly of DNA molecules up to several hundred kilobases. *Nat Methods* **6**, 343–345 (2009).

31. C. Engler, R. Kandzia, S. Marillonnet, A one pot, one step, precision cloning method with high throughput capability. *PLoS One* **3**, e3647 (2008).

32. O. T. Tuck, *et al.*, Hachiman is a genome integrity sensor. *bioRxiv* (2024).

33. N. Jia, *et al.*, Structures and single-molecule analysis of bacterial motor nuclease AdnAB illuminate the mechanism of DNA double-strand break resection. *Proc Natl Acad Sci U S A* **116**, 24507–24516 (2019).

34. K. Cheng, M. Wilkinson, Y. Chaban, D. B. Wigley, A conformational switch in response to Chi converts RecBCD from phage destruction to DNA repair. *Nat Struct Mol Biol* **27**, 71–77 (2020).

35. A. Punjani, J. L. Rubinstein, D. J. Fleet, M. A. Brubaker, cryoSPARC: algorithms for rapid unsupervised cryo-EM structure determination. *Nature Methods* **14**, 290–296 (2017).

36. H. Cao, *et al.*, EMReady2: improvement of cryo-EM and cryo-ET maps by local quality-aware deep learning with Mamba. *Nat Commun* (2026). https://doi.org/10.1038/s41467-026-71794-1.

37. J. Jumper, *et al.*, Highly accurate protein structure prediction with AlphaFold. *Nature* **596**, 583–589 (2021).

38. E. F. Pettersen, *et al.*, UCSF ChimeraX: Structure visualization for researchers, educators, and developers. *Protein Sci* **30**, 70–82 (2021).

39. P. Emsley, B. Lohkamp, W. G. Scott, K. Cowtan, Features and development of Coot. *Acta Crystallogr D Biol Crystallogr* **66**, 486–501 (2010).

40. T. I. Croll, ISOLDE: a physically realistic environment for model building into low-resolution electron-density maps. *Acta Crystallogr D Struct Biol* **74**, 519–530 (2018).

41. D. Liebschner, *et al.*, Macromolecular structure determination using X-rays, neutrons and electrons: recent developments in Phenix. *Acta Crystallogr D Struct Biol* **75**, 861–877 (2019).

42. V. B. Chen, *et al.*, MolProbity: all-atom structure validation for macromolecular crystallography. *Acta Crystallogr D Biol Crystallogr* **66**, 12–21 (2010).

43. M. S. Dillingham, S. C. Kowalczykowski, RecBCD enzyme and the repair of double-stranded DNA breaks. *Microbiol Mol Biol Rev* **72**, 642–71, Table of Contents (2008).